Chapter 3

A NEAR-EQUILIBRIUM COUPLED MECHANISTIC MODEL FOR CALCITE DISSOLUTION IN SEAWATER WITH 0, 14, AND 28 MILLIMOLAR TOTAL SULFATE

3.1 Introduction

Calcite dissolution kinetics have historically been fit using the empirical equation:

$$R = k(1 - \Omega)^n \quad (3.1)$$

Here, k is the rate constant (mol cm^{-2} s^{-1}), $\Omega = \frac{[Ca^{2+}][CO_3^{2-}]}{K'_{sp}}$ such that 1-Ω is a measure of the thermodynamic driving force of the solution, and n is a reaction order that varies from ~1 in low ionic strength water (Arakaki and Mucci, 1995; Boudreau, 2013; Cubillas et al., 2005; Sulpis et al., 2017; Svensson and Dreybrodt, 1992), to ~3-4.5 in seawater (Dong et al., 2018; Keir, 1980; Morse, 1978; Morse and Berner, 1972; Naviaux et al., 2019b, 2019a; Subhas et al., 2015, 2017; Walter and Morse, 1985). The simplicity of Eq. 1 has led to its widespread use in the mineral dissolution community, but this simplicity comes at the cost of mechanistic interpretability.

Calcite dissolution kinetics may be broadly broken down into four interrelated pieces: 1) the thermodynamic driving force of the solution (Ω), 2) the chemical speciation of the solution, 3) the chemical speciation of the mineral surface, and 4) the active surface dissolution mechanism (i.e. whether dissolution is dominated by the retreat of pre-existing steps, the formation of etch pits at defects, or the formation of etch pits homogenously across the mineral surface). We distinguish between each aspect in our discussion, but their effects on the overall dissolution rate are intertwined. As an example, changing the solution composition may alter the dissolution rate through changes in Ω, through changes in the mineral surface speciation, or through both simultaneously. Ultimately, the goal is to create

a unified theory of mineral dissolution that captures the complex relationships between each of the above mechanistic pieces.

Studies of calcite dissolution in low ionic strength water have made the most progress towards a unified mechanistic theory. Early research identified three rate-controlling chemical reactions in solution, that when combined, recreated the linear (n = 1 in Eq. 3.1) relationship of calcite dissolution rate versus Ω in freshwater (Busenberg and Plummer, 1986; Chou et al., 1989; Plummer et al., 1979a, 1978):

$$\mathrm{CaCO_{3(s)}} + \mathrm{H^+} \rightarrow Ca^{2+} + \mathrm{HCO_3^-} \quad (3.2a)$$

$$\mathrm{CaCO_{3(s)}} + \mathrm{H_2CO_3} \rightarrow Ca^{2+} + 2\mathrm{HCO_3^-} \quad (3.2b)$$

$$\mathrm{CaCO_{3(s)}} + \mathrm{H_2O} \rightleftharpoons Ca^{2+} + CO_3^{2-} + \mathrm{H_2O} \quad (3.2c)$$

In acidic conditions (pH <5), calcite dissolution exhibits a first order dependence on the activity of hydrogen ion in solution (Eq. 3.2a). H_2CO_3 is a neutral molecule that may also act as a proton donor and whose contribution to the overall rate becomes important in more basic conditions and at higher pCO_2 levels (Eq. 3.2b). Water catalyzed dissolution is thought to be constant and independent of solution chemistry, as the activity of the solid is assumed to be one (Eq. 3.2c).

In addition to pure solution chemistry, another avenue of research focused on understanding calcite dissolution in terms of reactive sites (Berner and Morse, 1974) and complexes on the mineral surface (Amrhein et al., 1985; Sjöberg and Rickard, 1984b). X-ray photoelectron spectroscopy provided direct evidence of a hydrated layer at the calcite surface (Stipp and Hochella, 1991), and adsorbed OH^-, HCO_3^-, Ca^{2+}, and CO_3^{2-} were identified as important precursors controlling the rate of dissolution near equilibrium (Busenberg and Plummer, 1986). With these results in mind, Van Cappellen et al. (1993) developed a constant capacitance model (CCM) of calcite surface complexation. In this model, dissolved cations/anions in solution adsorb at the mineral-solution interface (the “0-plane”) by

exchanging H^+/OH^- at hydroxylated cation sites (>Ca-OH^0) or protonated anion sites (>CO_3-H^0). Note that "*>i*" represents an ion associated with the mineral lattice. A key assumption in the Van Cappellen model is that formation of surface complexes is fast, and their detachment sets the dissolution rate. The model recreated observed trends in calcite surface charge versus pH and was able to correlate calcite dissolution rates at $\Omega = 0$ with densities of surface species.

In one of the most influential papers in the field, Arakaki and Mucci (1995) coupled the Van Cappellen et al. CCM with Eq.'s 3.2a-c to suggest the following reactions between surface complexes and ions in solution:

$$> CO_3^- + 2H^+ \underset{k_5}{\overset{k_1}{\rightleftarrows}} > Ca^+ + H_2CO_3 \tag{3.3a}$$

$$> Ca^+ + H_2CO_3 \underset{k_6}{\overset{k_2}{\rightleftarrows}} > CO_3H + CaHCO_3^+ \tag{3.3b}$$

$$> CO_3H + CaHCO_3^+ \underset{k_7}{\overset{k_3}{\rightleftarrows}} > Ca^+ + H_2CO_3 + CaCO_3^0 \tag{3.3c}$$

$$CaCO_{3(Solid)} \underset{k_8}{\overset{k_4}{\rightleftarrows}} CaCO_3^0 \tag{3.3d}$$

which could be combined into the complete rate equation:

$$\text{Rate} = k_1 > CO_3^-\{H^+\}^2 + (k_2 - k_5) > Ca^+\{H_2CO_3^*\} + k_4 - (k_6 - k_3) > CO_3H\{CaHCO_3^+\} - k_7 > Ca^+\{H_2CO_3^*\}\{CaCO_3^0\} - k_8\{CaCO_3^0\} \tag{3.4}$$

Here, > *i* is the density of surface complex *i* (mol m^{-2}), $\{i\}$ is the activity of dissolved species *i*, and k_i is the rate constant for reaction *i* in Eq.'s 3.3a-d.

By including the activities of ions in solution alongside the densities of surface complexes, the Arakaki and Mucci model, hereafter referred to as the A&M model, successfully fit freshwater calcite dissolution rates from $0.8 > \Omega > 0$ over a wide range of pCO_2 and pH. The A&M model also reproduced far-from-equilibrium rate behavior observed in bulk dissolution studies. In acidic (pH < 5) conditions, Eq. 3.4 reduces to a linear rate versus H^+ relationship as all $>CO_3^-$ are protonated to $>CO_3H$ and the k_1 term dominates. In more alkaline conditions, Eq. 3.4 is linear versus Ω. Another convincing aspect of the model is that the fitted values of $\frac{k_4}{k_8\{CaCO_3^0\}}$ provide an excellent estimate of calcite K_{sp} in freshwater.

The A&M model was able to describe dissolution rates without accounting for variations in surface dissolution mechanism, but this success may have been a function of the data used to validate the model. The existence of different surface mechanisms was well known at the time of A&M (Burton et al., 1951; Burton and Cabrera, 1949; Cabrera and Levine, 1956; Lasaga and Blum, 1986; MacInnis and Brantley, 1992; Schott et al., 1989; Zhang and Nancollas, 1990), but it was not until Teng (2004) that the "critical Ωs" ($\Omega_{critical}$s) for activating each mechanism were well constrained. Teng found that calcite dissolution in low ionic strength water proceeded by the retreat of pre-existing steps for $1 > \Omega > 0.54$, 2D etch pit formation at defects for $0.54 > \Omega > 0.007$, and finally homogenous 2D etch pit formation for $0.007 > \Omega$. A&M validated their model on dissolution rates between $0.8 > \Omega > 0$ from Plummer et al. (1978), and A&M state that they recreate the linear rate behavior versus 1-Ω. However, it is unclear from the figures in A&M how well the model actually fits the raw data on the extreme ends of the Ω range. The original data in Plummer et al. (1978) does not include Ω calculations, so we instead plot in Figure 3.1 the data from another paper by the same authors using the same pH stat method (Busenberg and Plummer, 1986). It is clear from this raw data that the linear behavior does not extend for the entire Ω range. All dissolution rates begin to fall off the linear trend around $\Omega > 0.5$, where calcite transitions from defect-assisted etch pit formation to pure step-retreat. There is also a large increase in the dissolution rate near $1\text{-}\Omega \sim 1$ that is likely due to the activation of homogenous etch pit formation. We therefore hypothesize that the fitted rate constants in the A&M were derived

primarily from calcite dissolving via a single surface mechanism, defect-assisted etch pit formation.

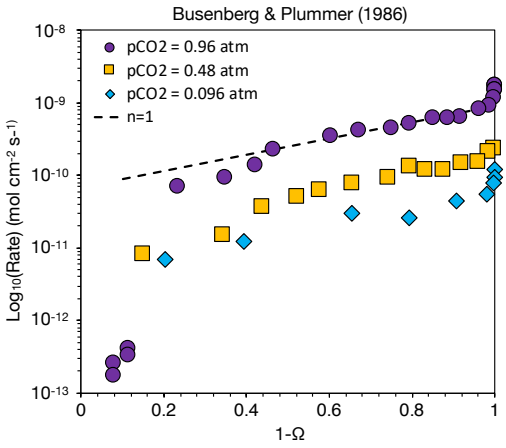

Figure 3.1: Data transcribed from Table 10 of Busenberg and Plummer (1986) on calcite dissolution rates (mol cm^{-2} s^{-1}) versus 1-Ω in $Ca(HCO_3)_2$ solutions at different pCO_2 levels. The n = 1 line is a fit to Rate = k(1-Ω) using a k of $9 \cdot 10^{-10}$ mol cm^{-2} s^{-1}.

A mechanistic understanding of calcite dissolution in seawater has progressed more slowly than it has in freshwater, but several recent advances have helped to close the gap. Naviaux et al. (2019b) measured the near-equilibrium temperature dependence of calcite dissolution rates and demonstrated that the $\Omega_{critical}$s in seawater occurred much closer to equilibrium than they did in freshwater. Naviaux et al also provided the first estimates in seawater of the step kinetic coefficient (β), density of active nucleation sites (n_s), step edge free energy (α), activation energy of detachment from kinks/steps (ϵ_{step}), and activation energy of etch pit initiation (ϵ_{init}). Though β, n_s, ϵ_{step}, and ϵ_{init} had similar values to those reported in freshwater, the temperature dependence of α reversed sign depending upon which surface dissolution mechanism was active, suggesting a complete theory of calcite dissolution kinetics would require knowledge of the chemical speciation of the solution and/or mineral surface.

The solution speciation of seawater is notoriously complex, but recent advances have allowed for changes in speciation resulting from different major ion compositions to be

calculated (Hain et al., 2015). Historically, seawater speciation has been calculated using either a "bottom up" or "top down" approach. In the bottom up approach, thermodynamic parameters from freshwater experiments are adjusted to the desired conditions using ionic strength and interaction corrections (Millero and Pierrot, 1998; Millero and Schreiber, 1982; Pitzer, 1973). This strategy is used by the U.S Geological Survey modeling software, PHREEQC (Parkhurst, 1995), and has the advantage that it can be applied to solutions of varying compositions. However, the bottom up approach is more accurate in low to mid ionic strength conditions than in seawater (Hain et al., 2015). The top down approach used by programs such as CO2SYS (van Heuven et al., 2011) only considers the empirically determined values for association constants in seawater. CO2SYS provides the best estimates for modern seawater chemistries, but cannot be applied to alternative compositions that may have existed in the past. The MyAMI model released by Hain et al., (2015) combines the strength of each approach by using the Pitzer equations (Pitzer, 1973) to calculate changes in seawater association constants *relative* to empirically determined values:

$$\mathrm{pK}^*_{\mathrm{predicted}}|_{(\mathrm{T,S,X})} = \mathrm{pK}^*_{\mathrm{empirical}}(\mathrm{T,S})|_{\mathrm{X}_0} + \Delta\mathrm{pK}^*_{\mathrm{MyAMI}}|_{(\mathrm{T,S,X})} \quad (3.5a)$$

$$\Delta\mathrm{pK}^*_{\mathrm{MyAMI}}|_{(\mathrm{T,S,X})} = \mathrm{pK}^*_{\mathrm{MyAMI}}(\mathrm{T,S,X}) - \mathrm{pK}^*_{\mathrm{MyAMI}}(\mathrm{T,S,X}_0) \quad (3.5b)$$

Here, pK^* is the negative logarithm of the association constant, K^*. The "*" signifies that the constant is empirical and conditional on the temperature (T), salinity (S), and chemical composition (X) of the solution. X_0 is modern seawater composition.

Surface complexation models are widespread for calcite in low ionic strength water (Heberling et al., 2011; Oleg S. Pokrovsky et al., 2009; Pokrovsky, 1998b; Pokrovsky et al., 2005; Pokrovsky and Schott, 2002; Wolthers et al., 2012b, 2008), and generally come in two forms, simple CCMs such as the one in Van Cappellen et al. (1993), and more complex Stern models (SMs). In a CCM, all potential determining ions (PDIs) may coordinate with the 0-plane hydrolysis layer at the mineral surface. CCMs can account for a wide range of dissolution/precipitation rate behaviors (Schott et al., 2009), but they tend to overestimate the mineral surface capacitance (Heberling et al., 2011) and the effect of pH (Al Mahrouqi

et al., 2017). SMs provide a more realistic estimate of surface capacitance than CCMs, but they do so at the cost of model complexity. In addition to the surface hydrolysis layer, SMs explicitly model the inner (1-plane) and outer (2-plane) Helmholtz planes. Both SMs and CCMs are validated using surface potential measurements. However, the differences in sophistication between SMs and CCMs mean that the surface complexes proposed by each model differ greatly. SMs and CCMs have recently been extended to seawater solutions (Ding and Rahman, 2018; Song et al., 2019, 2017), but they have yet to be coupled with dissolution/precipitation rate data.

The goal of this paper is to combine the latest solution and surface chemistry models to test if the reactions proposed by A&M can also describe calcite dissolution rates in seawater. We achieve this by fitting Eq. 3.4 to the dissolution data from Naviaux et al. (2019b), as well as to novel dissolution rate measurements made in artificial seawater of varying total sulfate (SO_{4T}) concentrations. The sulfate experiments serve dual purposes: 1) Marine sulfate levels have varied between 0.1 and 28 mM over the last 3.5 billion years (Canfield and Farquhar, 2009; Fakhraee et al., 2019; Luo et al., 2010). Some work has shown that sulfate inhibits calcite dissolution rates far from equilibrium (Sjöberg, 1978), these results are not applicable to ocean saturations which are typically much closer to equilibrium. Given the changes in surface dissolution mechanism that occur near equilibrium (Naviaux et al., 2019b; Subhas et al., 2017), it is important to evaluate the effects of sulfate across the full range of Ω. 2) The sulfate data provides additional constraints on the A&M model fit, thereby allowing for a more robust test of the model.

3.2 Experimental Methods

Dissolution rate measurements were made by dissolving pure ^{13}C inorganic calcite in solutions of varying compositions according to previous methods (Dong et al., 2019, 2018; Naviaux et al., 2019a, 2019b; Subhas et al., 2015, 2017). All rate data for this manuscript were collected using ^{13}C-calcite that had been wet sieved to a size fraction of 20-53 μm, the specific surface area of which was established using Kr gas BET to be 0.152 ± 0.006 $m^2\ g^{-1}$ (Naviaux et al., 2019a, 2019b). Experiments were conducted in either Dickson Seawater

Reference Material (Dickson, 2010) or in phosphate free, "Aquil," artificial seawater (Morel et al., 1979) with varying concentrations of sulfate (Table 3.1) The ionic strengths of the Aquil solutions were held constant by compensating changes in sulfate with KCl. KCl was used because its components do not directly interact with the carbonic acid system species. Solution saturation states were calculated using pairs of alkalinity (Alk) and dissolved inorganic carbon (DIC) measurements as input parameters in either CO2SYS v1.1 (van Heuven et al., 2011), or a modified version of CO2SYS discussed below. Dickson seawater Ω was calculated with the carbonic acid system K_1' and K_2' dissociation constants from the Lueker et al. (2000) refit to Mehrbach et al.'s (1973) data, calcite K_{sp}' from Mucci (1983), K_{HSO4} from Dickson (1990a), and K_{boron} from Dickson (1990). The total boron-salinity ratio was taken from Lee et al., (2010). The standard errors in DIC (± 2-4 μmol kg^{-1}) and alkalinity (± 1-3 μmol kg^{-1}) were propagated using a Monte Carlo approach (Subhas et al., 2015), yielding final errors on Ω of 0.01-0.04 units.

Table 3.1: Composition of "Aquil" Artificial Seawater

	Composition (mol kg^{-1})		
Compound	Full Seawater	14 mM SO_{4T}	0 mM SO_{4T}
NaCl	$4.0976 \cdot 10^{-1}$	$4.0976 \cdot 10^{-1}$	$4.0976 \cdot 10^{-1}$
$CaCl_2 \cdot 2H_2O$	$1.029 \cdot 10^{-2}$	$1.029 \cdot 10^{-2}$	$1.029 \cdot 10^{-2}$
KBr	$8.2 \cdot 10^{-4}$	$8.2 \cdot 10^{-4}$	$8.2 \cdot 10^{-4}$
NaF	$7 \cdot 10^{-5}$	$7 \cdot 10^{-5}$	$7 \cdot 10^{-5}$
KCl	$9.160 \cdot 10^{-3}$	$2.316 \cdot 10^{-2}$	$3.716 \cdot 10^{-2}$
H_3BO_3	$4.73 \cdot 10^{-4}$	$4.73 \cdot 10^{-4}$	$4.73 \cdot 10^{-4}$
Na_2SO_4	$2.81 \cdot 10^{-2}$	$1.40 \cdot 10^{-2}$	0
$NaHCO_3$	$2.32 \cdot 10^{-2}$	$2.32 \cdot 10^{-2}$	$2.32 \cdot 10^{-2}$
$SrCl_2 \cdot 6H_2O$	$6.2 \cdot 10^{-5}$	$6.2 \cdot 10^{-5}$	$6.2 \cdot 10^{-5}$
$MgCl_2 \cdot 6H_2O$	$5.288 \cdot 10^{-2}$	$5.288 \cdot 10^{-2}$	$5.288 \cdot 10^{-2}$

3.3 Background and Modification of MyAMI Code

We briefly discuss the origin of the seawater speciation calculations our model is based upon, before discussing the modifications that we made. The original MIAMI model (Millero and

Pierrot, 1998) utilizes the Pitzer equations (Pitzer, 1973) to calculate the activity coefficients and equilibrium constants for seawater of arbitrary composition. In their "MyAMI" model, Hain et al. (2015) modified MIAMI to: 1) Use a truncated version of the general Pitzer equation ignoring higher order electrostatic terms. 2) Only consider the interactions of a subset of chemical species (Na^+, Cl^-, Mg^{2+}, SO_4^{2-}, HSO_4^-, Ca^{2+}, Sr^{2+}, K^+, $MgOH^+$, $B(OH)_4^-$, H_3BO_3, H_2CO_3, HCO_3^-, CO_3^{2-}, H^+, OH^-) deemed most relevant to the carbonic acid system equilibrium constants. 3) Calculate the change in equilibrium constants relative to empirically determined values, rather than deriving the equilibrium from activity calculations. Note that empirical equilibrium constants for the carbonic acid system are defined using "Total" concentrations of each species, where:

$$[HCO_3^-]_{Total} = [NaHCO_3] + [MgHCO_3^+] + [CaHCO_3^+] + [SrHCO_3^+] \quad (3.6a)$$

$$[CO_3^{2-}]_{Total} = [NaCO_3^-] + [MgCO_3] + [CaCO_3] + [SrCO_3] \quad (3.6b)$$

4) Derive equilibrium constants on the total pH (pH_T) scale, where $pH_T = -\log_{10}([H^+]_T) = -\log_{10}([H^+]_{Free} + [HSO_4^-])$. 5) Run more efficiently using a least square optimization algorithm to fit the equilibrium constants.

The MyAMI code takes as inputs temperature (T), salinity (S), and seawater composition (X). Concentrations of calcium ($[Ca^{2+}]$) and magnesium ($[Mg^{2+}]$) may be varied by the user, whereas total sodium, potassium, strontium, chloride, boron, and sulfate are assumed to vary with salinity according to the ratios in Table 4 of Millero et al. (2008). For a given T, S, $[Ca^{2+}]$, and $[Mg^{2+}]$, MyAMI outputs the change in the empirical equilibrium constants, ΔpK^*_{MyAMI}, such that the predicted equilibrium constant is given by Eq. 3.5a.

We further modified the MyAMI code for the analysis in this manuscript. We refer to this modified code as "Mod-MyAMI". The first modification, as recommended by Hain et al., (2016), was to update the Pitzer-model calcium-bicarbonate coefficients from those in Table 1 of Harvie et al. (1984), to those in Table 5 of He and Morse (1993). The second

modification was to remove the salinity dependence of [SO_{4T}] so that its concentration could be explicitly varied by the user. All code is available at https://github.com/jnaviaux/Sulfur_PyMyAMI.

Empirical equilibrium constants were calculated for seawater of modern composition, as well as for seawater with SO_{4T} = 14 mM, and SO_{4T} = 0 mM. The resulting values are in Table 3.2. These updated pK values were input into CO2SYS alongside Alk-DIC pairs to calculate Ω in Aquil seawater.

Table 3.2: Outputs from Mod-MyAMI Code. pK^* values are on the pH_T scale. γ^T and γ^F represents the "total" and "free" ion activity coefficients, respectively

Equilibrium Constant	$pK^*\|_{(28\ mM\ SO_{4T})}$	$pK^*\|_{(14\ mM\ SO_{4T})}$	$pK^*\|_{(0\ mM\ SO_{4T})}$
$K_w^* = [H^+]_T[OH^-]_T = K_w \frac{1}{\gamma_H^T \gamma_{OH}^T}$	13.217	13.274	13.337
$K_0^* = \frac{[H_2CO_3^*]}{CO_2} = K_0 \frac{\gamma_{CO_2}^F}{\gamma_{H_2CO_3}^F}$	1.547	1.545	1.543
$K_1^* = \frac{[H^+]_T[HCO_3^-]_T}{[H_2CO_3^*]} = K_1 \frac{\gamma_{H_2CO_3}^F}{\gamma_H^T \gamma_{HCO_3}^F}$	5.847	5.899	5.957
$K_2^* = \frac{[H^+]_T[CO_3^{2-}]_T}{[HCO_3^-]_T} = K_2 \frac{\gamma_{HCO_3}^F}{\gamma_H^T \gamma_{CO_3}^F}$	8.966	9.022	9.085
$K_{HSO4}^* = \frac{[H^+]_T[SO_4^{2-}]}{[HSO_4^-]} = K_{HSO_4} \frac{\gamma_{HSO_4}^F}{\gamma_H^T \gamma_{SO_4}^F}$	0.999	1.050	1.107[A]
$K_B^* = \frac{[H^+]_T[B(OH)_4^-]}{[H_3BO_3]} = K_B \frac{\gamma_{H_3BO_3}^F}{\gamma_H^T \gamma_{B(OH)_4}^F}$	8.598	8.648	8.705
$K_{spA}^* = \frac{[CO_3^{2-}]_T[Ca^{2+}]}{\Omega_{aragonite}} = K_{spA} \frac{1}{\gamma_{CO_3}^T \gamma_{Ca}^F}$	6.188	6.193	6.198
$K_{spC}^* = \frac{[CO_3^{2-}]_T[Ca^{2+}]}{\Omega_{calcite}} = K_{spC} \frac{1}{\gamma_{CO_3}^T \gamma_{Ca}^F}$	6.369	6.374	6.379

[A] Although this value was calculated, it was not necessary for the 0mM SO_{4T} experiments

3.4 Implementation into PHREEQC

3.4.1 Comparison with CO2SYS

PHREEQC is often used for speciation calculations, but it performs poorly when applied to seawater-like compositions (Hain et al., 2015). To demonstrate this, we compare the carbon

chemistry outputs from PHREEQC and CO2SYS in Figure 3.2. When using the default PHREEQC database, the equilibrium between $H_2CO_3^*$ and $HCO_3^-{}_T$ is offset by ~0.05 log units compared to its empirically determined value in seawater, and the equilibrium between $HCO_3^-{}_T$ and $CO_3^{2-}{}_T$ is offset by ~0.1 units.

Although sufficient for general use, this difference in carbonate speciation has a profound effect on the calculated calcite saturation state (Figure 3.2b,c). The Ω calculated by CO2SYS (Ω_{CO2SYS}) was used as a benchmark with which to compare the Ω calculated by PHREEQC ($\Omega_{PHREEQC}$). In both cases, DIC was set to 2 mM, and the solution saturation state was varied by changing pH_T. Under conditions where $\Omega_{CO2SYS} = 1$, the default PHREEQC database greatly underestimates the solution saturation and calculates $\Omega_{PHREEQC} = 0.68$. Updating the PHREEQC database to use the empirical seawater $pK_{spC}^* = 6.369$ (Mucci, 1983b) improves the discrepancy, but the offset between $\Omega_{PHREEQC}$ and Ω_{CO2SYS} still reaches 0.16 units when $\Omega_{CO2SYS} = 1$ (Figure 3.2c). Seawater calcite dissolution experiences two surface mechanism changes within ~0.2 Ω units (Naviaux et al., 2019b), so the PHREEQC database require further modification before its results can be coupled with experimental dissolution rates.

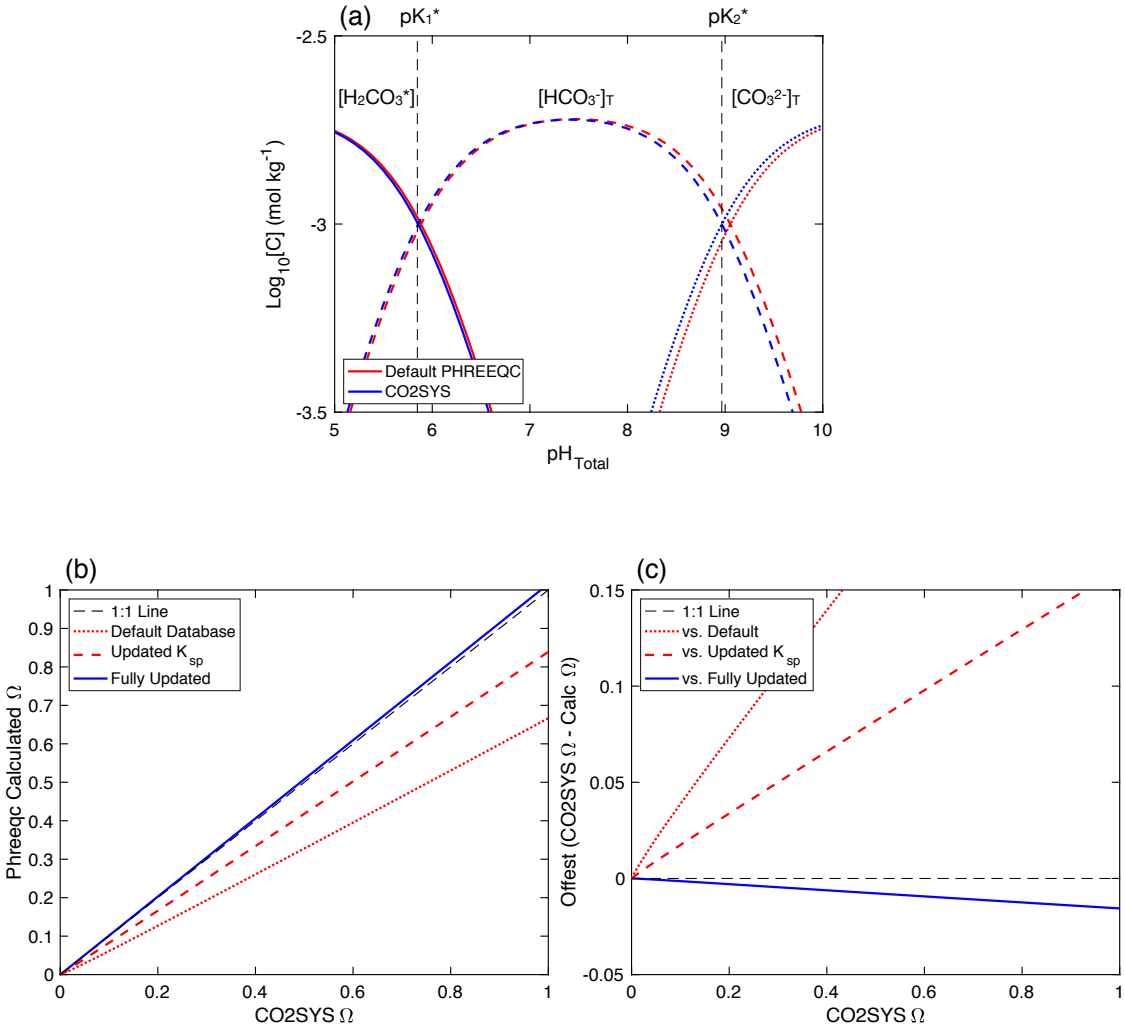

Figure 3.2: (a) Log_{10}Concentration versus pH_T in seawater at T=25°C, S=35, total DIC = 2 mM, for $[H_2CO_3^*]$, $[HCO_3^-]_T$, and $[CO_3^{2-}]_T$ calculated using the default PHREEQC database (red), and an updated database using the constants in Table 3.2 (blue). Empirical seawater pK^* values are included for reference. The equilibrium between each species is offset towards higher pH values when computed by the default PHREEQC database. (b) Ω_{CO2SYS} versus $\Omega_{PHREEQC}$ calculated by different iterations of PHREEQC databases for DIC = 2 mM and varying pH_T. See text for details. (c) The offset between Ω calculations versus Ω_{CO2SYS}. Even with updated K_{sp}^*, the default PHREEQC database is over 0.15 Ω units offset from Ω_{CO2SYS}. The fully updated PHREEQC database agrees within 0.02 Ω units from $0 < \Omega < 1$.

Final agreement between Ω calculations was achieved by removing the individual carbon system ion pairing reactions (components in Eq. 3.6a, b) from the PHREEQC database and

calculating $HCO_3^{-}{}_T$ and $CO_3^{2-}{}_T$ using the empirical pK values in Table 3.2. Once the Ω calculation from PHREEQC agreed with that from CO2SYS, we could then use PHREEQC to calculate the surface and chemical speciation for each of our experimental measurements. Note that the pKs in Table 3.2 are based upon concentrations, so the updated PHREEQC database now calculates concentrations of solution species, rather than activities. The updated database also no longer calculates the $CaHCO_3^+$ and $CaCO_3^0$ ion pairs, both of which are important in the A&M model. We can circumvent this limitation by applying the ratio of $CaHCO_3^+/HCO_3^{-}{}_T$ and $CaCO_3^0/CO_3^{2-}{}_T$ calculated by the default PHREEQC database to our final output. In seawater over the full Ω range, the default PHREEQC database calculates that $CaHCO_3^+$ will be 2.2% of $HCO_3^{-}{}_T$, and $CaCO_3^0$ will be 12.4% of $CO_3^{2-}{}_T$. These ratios will be carried forward in our fitting of the A&M equations, but we recognize that this is an area of future model improvement.

3.4.2 Choice of Surface Speciation Model

Three different surface speciation models were evaluated: a CCM by Song et al. (2019, 2017), a CCM by Ding and Rahman (2018), and a SM by Ding and Rahman adapted from Heberling et al. (2011). Though each model was validated against calcite surface potential measurements in seawater, they envision very different speciations taking place at the mineral surface. We chose to proceed using the CCM from Ding and Rahman, as it was most similar to the Van Cappellen et al. model used by A&M (Table 3.3). Future work will need to test alternative rate equations against the other surface complexation models.

Table 3.3: Comparison of surface binding constants among complexation models			
	$Log_{10}K$ (25°C, 1 atm)		
Surface Binding Reaction	Van Cappellen et al. (1993) I = 0	Pokrovsky and Schott (2002) I = 0	Ding and Rahman (2018) 0.06 < I < 1.1
$> CaOH + H^+ \rightleftarrows > CaOH_2^+$	12.2	11.85	11.8
$> CaOH + CO_3^{2-} + 2H^+ \rightleftarrows > CaHCO_3^0 + H_2O$	24.15	23.50	N/A
$> CaOH_2^+ + SO_4^{2-} \rightleftarrows > CaSO_4^- + H_2O$	N/A	N/A	-2.10
$> CaOH_2^+ + CO_3^{2-} \rightleftarrows > CaCO_3^- + H_2O$	3.35	5.25	6.00
$> CO_3H \rightleftarrows > CO_3^- + H^+$	-4.9	-5.1	-5.1
$> CO_3^- + Ca^{2+} \rightleftarrows > CO_3Ca^+$	2.1	3.4	2.85
$> CO_3^- + Mg^{2+} \rightleftarrows > CO_3Mg^+$	N/A	N/A	0.68

3.5 Results and Discussion

3.5.1 Dissolution Experiments with Variable [SO_{4T}]

Experimentally measured calcite dissolution rates are plotted versus pH_T in Figure **3.3**a, and 1-Ω in Figure **3.3**b,c. In agreement with previous studies (Sjöberg, 1978), removing sulfate increases calcite dissolution rates far-from-equilibrium, with rates being ~2x faster in 0 mM S_T Aquil than in 28 mM S_T seawater. Decreasing SO_{4T} increases dissolution rates for pH_T < 7.2, but pH is a poor metric for differentiating rates near equilibrium, so the effects are not as obvious for pH_T > 7.2. When plotted versus 1-Ω, it is clear that the effects of changing SO_{4T} depend strongly on the distance from equilibrium (Fig. 3.2c,d). Dissolution rates are fastest in low SO_{4T} Aquil far-from-equilibrium, but the differences between each of the three media decrease from $Log_{10}(1-\Omega)$ = 0 to -0.3 (Ω = 0 to 0.5). As the saturation continues to increase, dissolution rates in low SO_{4T} Aquil surpass rates in 28 mM SO_{4T} Aquil. The decrease in dissolution rates does not appear to scale directly with the change in SO_{4T}. At $Log_{10}(1-\Omega)$ = -0.82 (Ω = 0.85), dissolution rates in 14 mM SO_{4T} Aquil are ~3-4x slower than in full seawater, but rates in 0 mM SO_{4T} Aquil are over 20x slower.

Changing [SO_{4T}] may also affect the $\Omega_{critical}$s for transitions between surface dissolution mechanisms, but more data will be required to know this with certainty. Dissolution rates in

full seawater form two straight lines in Log-Log space, with a change in slope at $Log_{10}(1-\Omega) = -0.6$ ($\Omega = 0.75$). Once this critical undersaturation is surpassed, etch pits are no longer limited to formation at defects, and instead begin opening homogenously across the calcite surface (Naviaux et al., 2019b). Similarly to full seawater, the slope of rate versus Ω for 14 mM SO_{4T} Aquil appears linear from $-1.25 < Log_{10}(1-\Omega) < -0.6$, suggesting that dissolution in this media also proceeds by defect-assisted etch pit formation. The difference between the magnitude of the slope in 28 mM and 14 mM SO_{4T} from $-1.25 < Log_{10}(1-\Omega) < -0.6$ suggests that decreasing SO_{4T} lead to an increase in the calcite surface step edge free energy (Naviaux et al., 2019b). Dissolution rates in 14 mM SO_{4T} Aquil also follow a relatively linear dependence with Ω farther from equilibrium, though there may be additional curvature near the rate crossover point at $Log_{10}(1-\Omega) = -0.3$.

Calcite dissolution rates in 0 mM SO_{4T} Aquil exhibit a similar kink in slope at $Log(1-\Omega) = -0.6$, but the behavior on either side of this Ω differs from the other solutions. The 0 mM SO_{4T} Aquil exhibits greater curvature across the full Ω range, such that it forms an "S" shaped pattern. The "S" shape is largely driven by two points; the near-equilibrium point at $Log_{10}(1-\Omega) = -1.22$ ($\Omega = 0.94$), and the rate crossover point at $Log_{10}(1-\Omega) = -0.3$. Due to signal drift of the Picarro CRDS, the point nearest equilibrium was within error of 0 dissolution rate. Even if this point is ignored, the rate behavior in sulfate free Aquil is still quite different than in full seawater. More data will be required to constrain the surface dissolution mechanism.

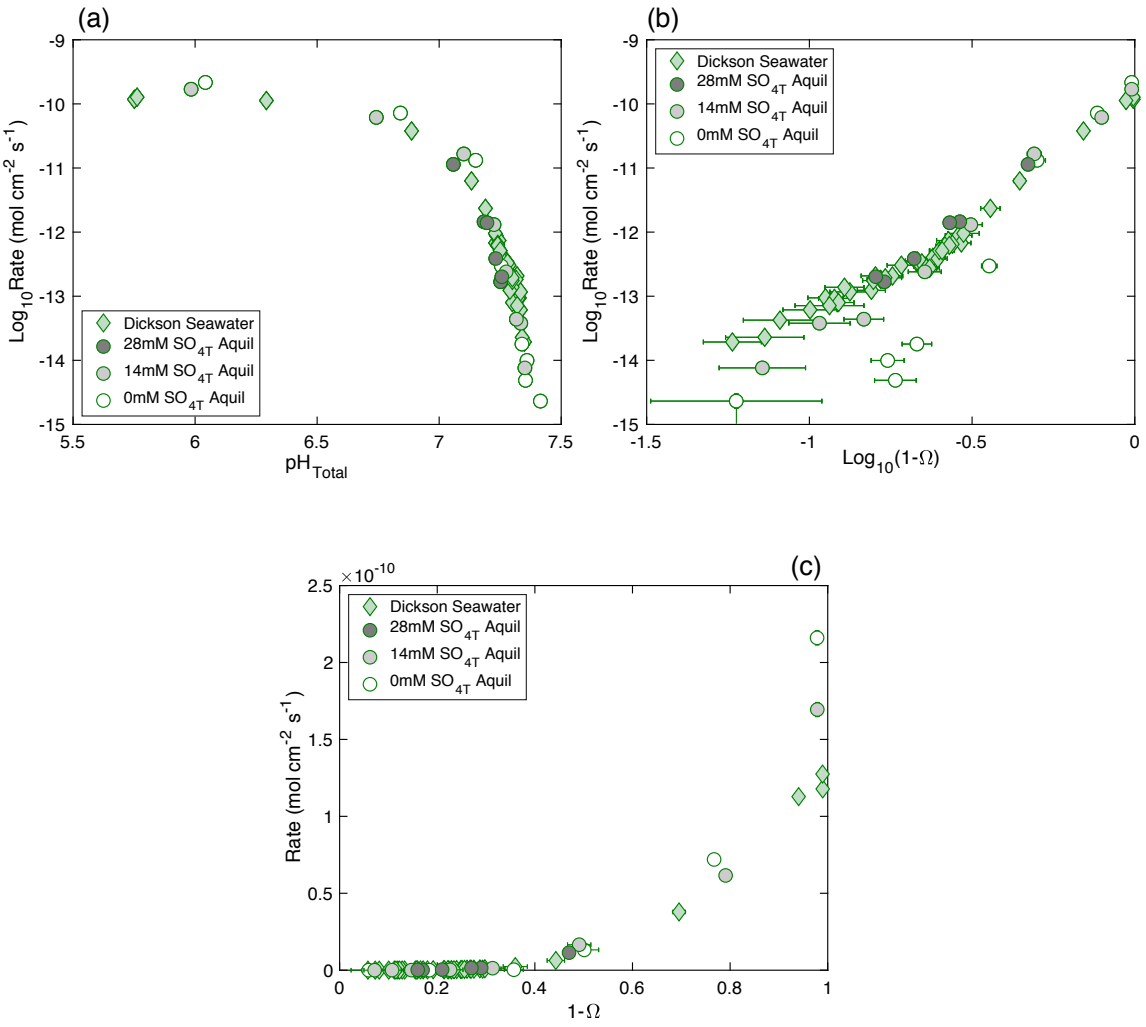

Figure 3.3: Dissolution rate (mol cm^{-2} s^{-1}) of inorganic calcite at 21°C in Dickson seawater (diamonds, 28 mM SO_{4T}, from Naviaux et al. 2019) and Aquil with 28 mM SO_{4T} (dark grey) 14 mM SO_{4T} (grey) or 0 mM SO_{4T} (open circles) plotted as (a) Log_{10}(Rate) vs. pH_T, (b) Log_{10}(Rate) vs. Log_{10}(1-Ω), (c) Rate vs. 1-Ω. Error bars are typically smaller than symbols. The 0 mM SO_{4T} point closest to equilibrium is within error of 0 dissolution rate.

3.5.2 Surface and Solution Speciation Calculations

The coupled PHREEQC speciation results for the bulk solution and calcite surface are plotted versus pH_T in Figure **3**.**4**a,b. Solution carbon speciation is plotted for each [SO_{4T}], but surface speciation is only plotted for 28 mM (solid lines) and 0 mM (dashed lines) SO_{4T} for visual clarity. We plot all surface species in the Ding and Rahman (2018) CCM, but focus our

discussion on $>CaOH_2^+$, $>CO_3^-$, and $>CO_3H$, as these species appear in Eq. 3.4. Similarly to freshwater, surface calcium and carbonate groups are dominated by $>CaOH_2^+$ and $>CO_3^-$ for $pH_T < 6$ (Figure **3.4**b). As the pH increases, $>CaOH_2^+$, $>CO_3^-$, and $>CO_3H$ are replaced by $>CaCO_3^-$ and $>CO_3Ca^+$ groups. The concentration of $>CO_3H$ decreases more rapidly than $>CaOH_2^+$ and $>CO_3^-$. Removing sulfate does change the distribution of surface species slightly, but the magnitude of the change is difficult to see given the nearly 7 order of magnitude spread in surface species concentrations. For the solution, removing sulfate shifts every pK^* towards higher values (Table 3.2), such that, at any given pH_T, there is more $[H_2CO_3^*]$, less $[HCO_3^-]_T$, and less $[CO_3^{2-}]_T$ (Figure **3.4**a).

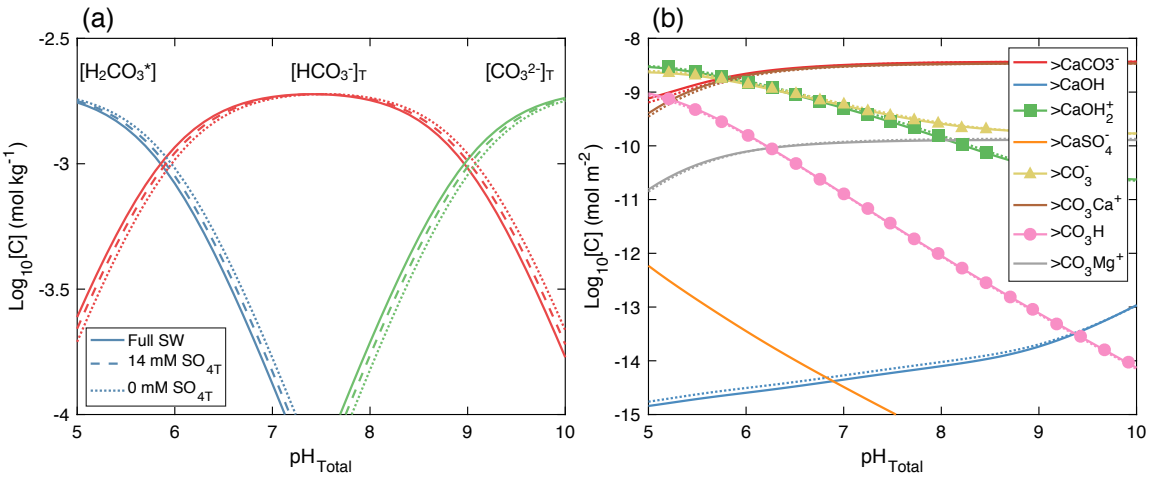

Figure 3.4: Log_{10}(Concentration) versus pH_T for (a) solution carbon speciation in 28 (solid lines), 14 (large dashes), and 0 mM (small dashes) SO_{4T} seawater and (b) mineral surface speciation in 28 (solid lines) and 0 mM SO_{4T} seawater. Symbols indicate surface species present in Eq. 3.4.

Removing sulfate necessarily affects pH_T by decreasing $[HSO_4^-]$, so changes in speciations are more informative when plotted versus Ω (Figure **3.5**a-c). Plotting versus Ω also facilitates comparisons with dissolution rate data near equilibrium. For the speciation of the surface, we see that complexes change by 1-2 orders of magnitude between $0 < \Omega < 0.1$, and then evolve more gradually as Ω approaches 1. Removing sulfate decreases $>CaOH_2^+$ and $>CO_3^-$ by ~3% and $>CO_3H$ by 26%, with the difference being nearly constant from $0.1 < \Omega < 1$

(Figure **3.5**c). For the solution speciation, normalizing by Ω reveals that carbon speciation is not affected by removing sulfate (Figure **3.5**a). However, the acidity of the solution, as measured by $[H^+]_T = [H^+]_F + [HSO_4^-]$, decreases by 22% when going from 28 to 0 mM SO_{4T} (Figure **3.5**b,c).

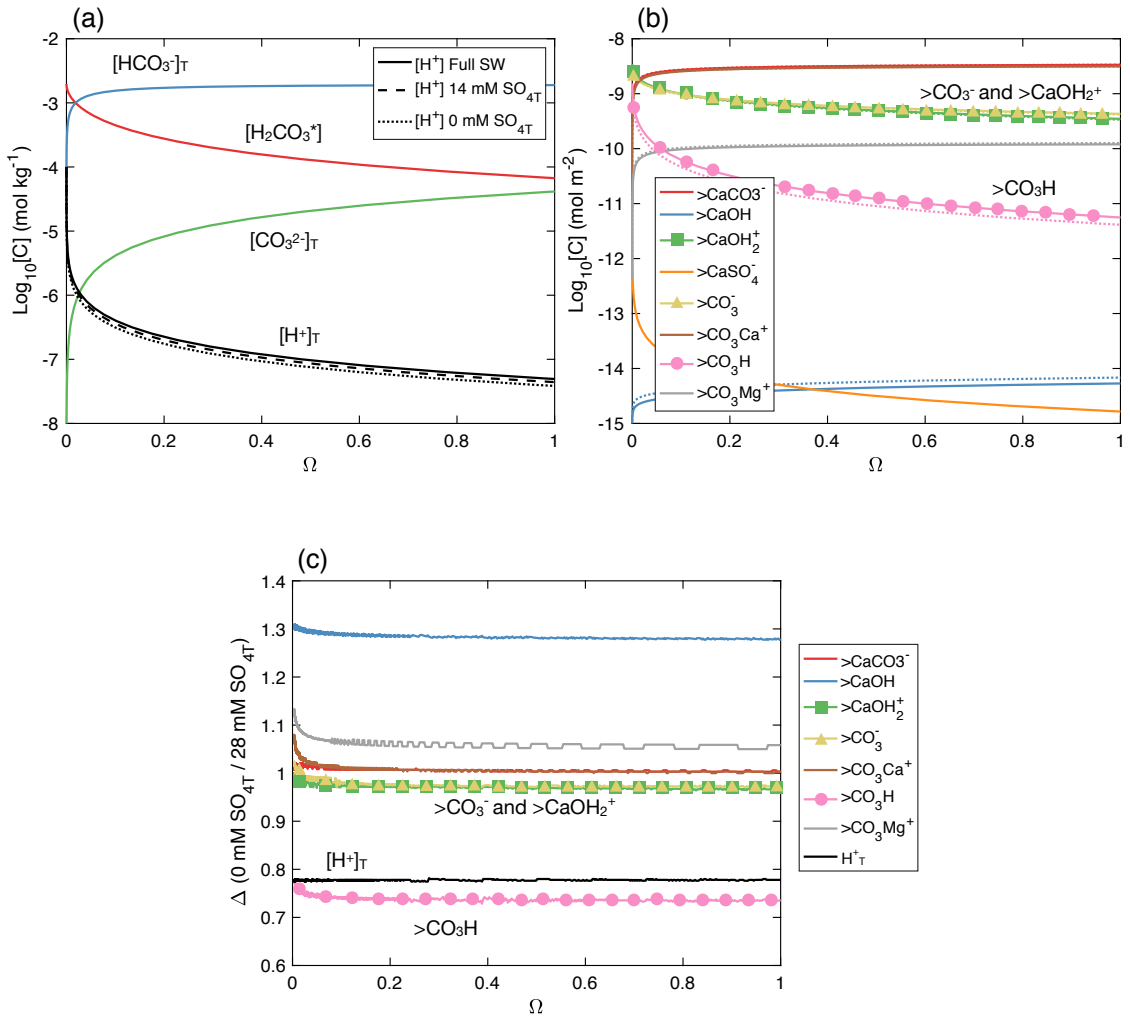

Figure 3.5: Log_{10}(Concentration) versus Ω for (a) solution carbon speciation in 28 (solid lines), 14 (large dashes), and 0 mM (small dashes) SO_{4T} seawater and (b) mineral surface speciation in 28 (solid lines) and 0 mM SO_{4T} seawater. (c) the relative difference between species concentrations in 0 mM and 28 mM SO_{4T} seawater versus Ω. Symbols indicate surface species present in Eq. 3.4.

3.5.3 Proposed Kinetic Model

The updated PHREEQC database was used to calculate $>CaOH_2^+$, $>CO_3^-$, $>CO_3H$, $[H_2CO_3^*]$, $[HCO_3^-]_T$, and $[CO_3^{2-}]_T$ at intervals of 0.001 Ω units from $0.01 < \Omega < 1$. Though not calculated explicitly, $[CaHCO_3^+]$ was taken to be 2.2% of $[HCO_3^-]_T$, and $[CaCO_3^0]$ was taken to be 12.4% of $[CO_3^{2-}]_T$ as discussed above. The calculated Ωs were used to match experimental dissolution rate data with the corresponding speciation calculations. The best fits to the rate constants in Eq. 3.4 were found using MATLAB's lsqnonlin least squares minimization function. Given initial estimates of rate constants, this function simultaneously minimized the difference between the measured and calculated dissolution rates in each solution. Dissolution rates corresponding with homogenous etch pit formation ($\Omega < 0.75$) could not be fit by Eq. 3.4, but the model successfully fit all data from $0.9 < \Omega < 0.75$ where dissolution in full SO_4 seawater occurs via defect-assisted etch pit formation. The success of this fit near equilibrium is impressive, as it indicates that the same chemical reactions set calcite dissolution rates in both freshwater and seawater for defect-assisted etch pit formation. The best fit parameters are in Table 3.4, and the predicted rates are plotted versus the experimental measurements in Figure 3.6.

Table 3.4: Best fit to rate constants in Eq. 3.4 when rate is expressed in mol cm^{-2} s^{-1} and surface species densities are in mol m^{-2}

Rate Constant	Units	This Study (Seawater, $0.75<\Omega<0.9$)	A&M (Freshwater)	Ratio (This Study / A&M)
k_1	s^{-1}	$6.17 \cdot 10^{8}$	$4.381 \cdot 10^{6}$	141
k_2-k_5	s^{-1}	$1.03 \cdot 10^{-7}$	42.52	$2.4 \cdot 10^{-9}$
k_4	mol cm^{-2} s^{-1}	$4.31 \cdot 10^{-12}$	$6.914 \cdot 10^{-11}$	$6.2 \cdot 10^{-2}$
k_6-k_3	s^{-1}	3.73	61.67	$6.0 \cdot 10^{-2}$
k_7	s^{-1}	$9.09 \cdot 10^{3}$	$2.332 \cdot 10^{5}$	$3.9 \cdot 10^{-4}$
k_8	mol cm^{-2} s^{-1}	$5.77 \cdot 10^{-8}$	$1.275 \cdot 10^{-5}$	$4.5 \cdot 10^{-3}$

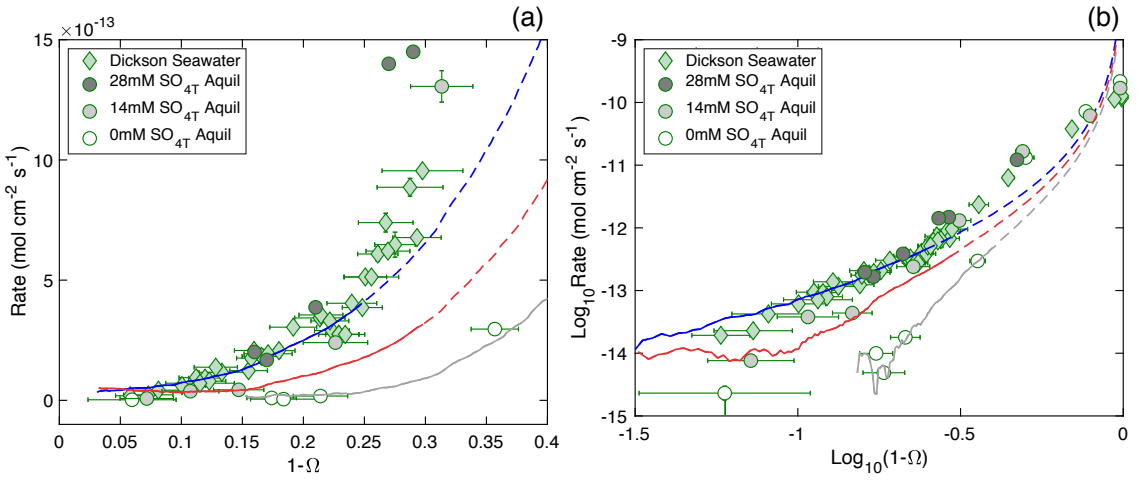

Figure 3.6: Fits of Eq. 3.4 to experimental rate (mol cm^{-2} s^{-1}) versus 1-Ω data in (a) linear axes and (b) Log-Log axes. Dissolution in Dickson seawater is fit by the blue curve, 14 mM SO_{4T} Aquil by the red curve, and 0 mM SO_{4T} Aquil by the grey curve. Data near equilibrium is well described by the model (solid lines), but extrapolating the fit to Ω = 0 (dashed lines) systematically misfits dissolution rates. Note that the chatter in the fits near equilibrium is because net dissolution is the difference between large gross dissolution and gross precipitation fluxes which have been calculated using interpolated speciation data.

As suggested by previous work (Subhas et al., 2017), dissolution rates in seawater result from the difference between large gross dissolution and precipitation fluxes. The contribution of each term in Eq. 3.4 to the overall dissolution rate is plotted in Fig. 3.7. The largest contributors to the forward rate are the k_1 and k_4 terms corresponding with attack of water and protons, respectively. Note that protons can be from H^+ or HSO_4^- in this model. The back reaction is set by k_7 and (k_6-k_3) terms, with a small contribution from the k_8 term. The (k_2-k_5) term for attack by $H_2CO_3^*$ is negligibly small.

One piece of evidence that A&M used to validate their fitted rate constants was to estimate the calcite solubility product, as $\frac{k_4}{k_8 K_{CaCO_3^0}} = \{Ca^{2+}\}\{CO_3^{2-}\} = K_{sp}^0$. We can do the same calculation using our fitted values along with the stoichiometric association constant for $CaCO_3^0$ in seawater (pK_{CaCO3} = 2.1 ± 0.1, Millero and Schreiber, 1982). Note that pK_{CaCO3} was not included in the full speciation model because of its effect on other ions in solution, but we use it here as it allows for a more accurate calculation. We recover a pK_{sp}^* of 6.23,

which is impressively close to the accepted value of 6.369 (Mucci, 1983b). The relative agreement between the calculated and known pK_{sp}^{*} values further supports the validity of our model.

Our fitted rate constants help to explain why changes in dissolution rate do not scale linearly with changes in $[SO_{4T}]$. We see from Fig X that removing sulfate lowers the gross forward rate via changes to the acidity of the solution, and the gross backwards rate via changes to the surface speciation. The k_1 term is multiplied by $[H+]_T^2$, and since the $[HSO_4^-]$ contribution to $[H+]_T$ falls with the removal of sulfate, the gross contribution of the k_1 term also falls. According to the speciation model, removing sulfate causes $>CO_3H$ sites to be replaced by $>CO_3Mg^+$ and $>CO_3Ca^+$ (Fig. 2.5c), thereby lowering the backwards (k_6-k_3) term in Eq. 3.4. The k_1 term decreases more rapidly than the (k_6-k_3) term, allowing for the net rate to scale non-linearly to the change in $[SO_{4T}]$.

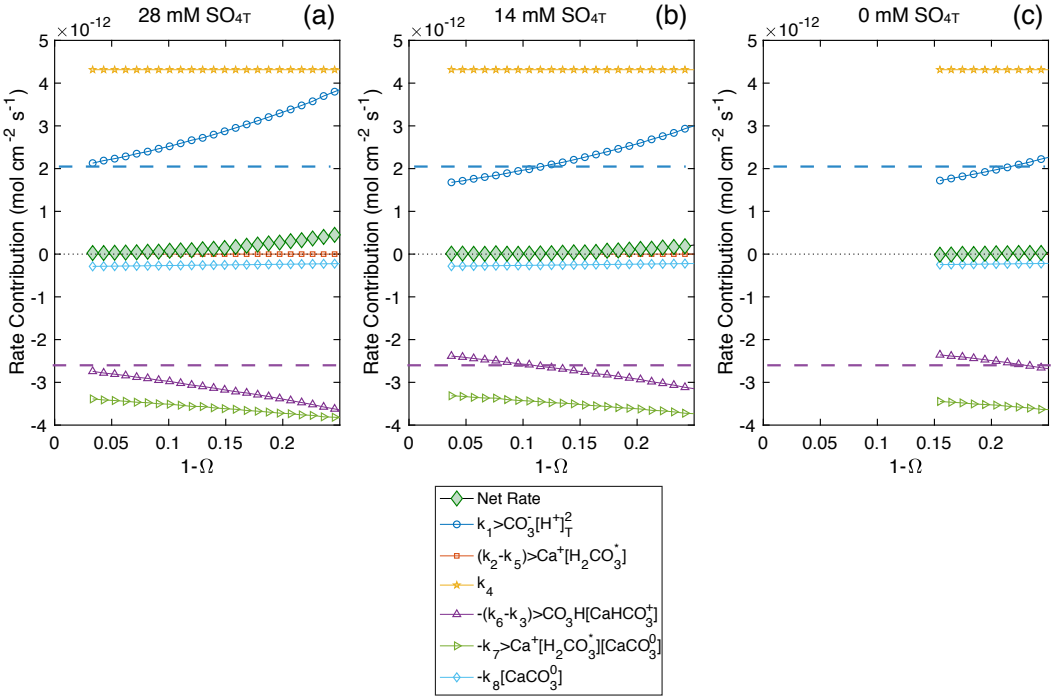

Figure 3.7: Contribution of each term of Eq. 3.4 to the overall dissolution rate in (a) Dickson seawater, (b) 14 mM SO_{4T} Aquil, and (c) 0 mM SO_{4T} Aquil. The "Net Rate" curves stop when the overall rate becomes negative. Horizontal dashed lines are provided to help see changes in the k_1 and k_6-k_3 terms between solution compositions.

3.5.4 Comparison of Model Fits in Seawater versus Freshwater

The most obvious difference when comparing fits between seawater and freshwater dissolution data is the Ω range for which Eq. 3.4 is valid. A&M fit dissolution rates from $0 < \Omega < 0.8$, whereas we are only able to fit a 0.15 Ω unit spread from $0.75 < \Omega < 0.9$ in seawater. Though the Ω ranges are much different, they approximately correspond with the same surface dissolution mechanism: defect-assisted etch pit formation. It is therefore valid to directly compare the fitted rate constants in Table 3.4.

With the exception of k_1, all rate constants are smaller in seawater than their corresponding values in freshwater (Table 3.4). This is consistent with the fact that calcite dissolves more slowly near equilibrium in seawater by >2 orders of magnitude (Naviaux et al., 2019b; Subhas et al., 2015). Though large, the magnitude of the seawater k_1 rate constant is borne

out of the measured dissolution rate changes from removing sulfate. Attempts to fit the data using a smaller k_1 value were unsuccessful.

Examining the fitted (k_2-k_5) terms suggests that the attack of $H_2CO_3^*$ is a vanishingly small contributor to the overall dissolution rate in seawater. This is an unexpected result, as carbonic anhydrase (CA), an enzyme that catalyzes the equilibration between $CO_{2(aq)}$ and $H_2CO_3^*$, has been shown to greatly increase seawater calcite dissolution rates near equilibrium (Subhas et al., 2017). It was thought that the mechanism of CA rate enhancement was through an increase in [$H_2CO_3^*$] availability, but this is challenged by our modeling results. Interestingly, the (k_2-k_5) term is the largest contributor to the overall dissolution rate in freshwater. This may be because the pCO_2 of the A&M experiments was very high ($0.2 < pCO_2$ (atm) < 1.0), leading to greater [$H_2CO_3^*$] than would occur under atmospheric pressures. However, more recent research has suggested that $H_2CO_3^*$ is irrelevant to freshwater calcite dissolution, and that pCO_2 affects the dissolution rate through changes in $>CaOH_2^+$ (Oleg S. Pokrovsky et al., 2009). Future research will be required to directly test the effect of $H_2CO_3^*$ on calcite dissolution.

Differences between freshwater and seawater dissolution may also be seen in the rate constants for the backwards reactions. A&M found that the (k_6-k_3) term was mainly responsible for lowering the dissolution rate from pH 5-6 for $pCO_2 = 0.97$ atm, but that the k_8 term was more important at lower pCO_2 (0.1 atm) or higher pH (>6.5). In seawater, we find that the k_7 and (k_6-k_3) terms contribute similarly to the backwards rate, with the (k_6-k_3) term becoming more important farther from equilibrium. The k_8 term contributes the least to the backwards reaction, likely because only ~12.4% of $CO_3^{2-}{}_T$ exists as $CaCO_3^0$ in seawater.

3.6 Summary and Conclusions

We measured calcite dissolution rates in artificial seawater of varying [SO_{4T}] across the full range of saturation states. We found that the effect of sulfate varied depending upon the distance from equilibrium. In agreement with previous studies (Sjöberg, 1978), removing sulfate increased the calcite dissolution rate by a factor of ~2 far from equilibrium ($\Omega \sim 0$). However, removing sulfate had the opposite effect for $\Omega > 0.5$, with calcite dissolution rates

in sulfate free seawater slowing by > 20x. The magnitude of rate inhibition did not scale directly with sulfate concentration. These finding have significant implications for calcite dissolution rates in ancient oceans, where sulfate concentrations were much lower than in the modern (Canfield and Farquhar, 2009; Fakhraee et al., 2019; Luo et al., 2010).

We used these dissolution measurements, along with the latest speciation models, to test if the same mechanistic rate equation developed for calcite dissolution in freshwater (Arakaki and Mucci, 1995) could also be applied to seawater. The equation is based upon four reversible reactions that capture the interaction between the solution and mineral surface chemistries. We successfully fit the equation to all of our rate measurements for $\Omega > 0.75$ using a least squares minimization technique. This Ω range corresponds with dissolution by defect-assisted etch pit formation (Naviaux et al., 2019b), which is likely the same mechanism that produced the data for the original freshwater model. We find that removing sulfate simultaneously decreases the gross forward *and* backwards rates, with the combined effect being a decrease in the net dissolution rate. Within the context of the model, the change in rate from removing sulfate is only possible if HSO_4^- is considered alongside H^+ as dissolution agents in the forward reaction. The validity of our model is supported by the fact that our fitted rate constants reproduce the value for calcite pK_{sp}^* in seawater.

Our model couples the effects of Ω with the speciations of the solution and mineral surface, and in doing so, successfully describes calcite dissolving via defect-assisted etch pit formation. We were unable to fit any of our data for $\Omega < 0.75$, where dissolution proceeds by homogenous etch pit formation. This discrepancy may be improved in the future by testing alterative models of surface speciation (Ding and Rahman, 2018; Song et al., 2019, 2017) and/or rate equations for far from equilibrium mineral dissolution (Lasaga and Lüttge, 2001; Lüttge, 2006).